
Article:
Irzal, F., Remmers, J.J.C., Huyghe, J.M. et al. (1 more author) (2013) A large deformation formulation for fluid flow in a progressively fracturing porous material. Computer Methods in Applied Mechanics and Engineering, 256. pp. 29-37. ISSN 0045-7825

https://doi.org/10.1016/j.cma.2012.12.011

A large deformation formulation for fluid flow in a progressively fracturing porous material

Faisal Irzal[1], Joris J. C. Remmers[1], Jacques M. Huyghe[2], René de Borst[3]

[1] *Department of Mechanical Engineering, Eindhoven University of Technology, PO BOX 513, 5600 MB, Eindhoven, The Netherlands*
[2] *Department of Biomedical Engineering, Eindhoven University of Technology, PO BOX 513, 5600 MB, Eindhoven, The Netherlands*
[3] *University of Glasgow, School of Engineering, Rankine Building, Oakfield Avenue, Glasgow G12 8LT, UK*

Abstract

A general numerical model has been developed for fluid flow in a progressively fracturing porous medium subject to large deformations. The fluid flow away from the crack is modelled in a standard manner using Darcy's relation, while in the discontinuity Stokes' flow is assumed, taking into account the change of permeability due to progressive damage evolution inside the crack. The crack is described in a discrete manner by exploiting the partition-of-unity property of finite element shape functions. The nucleation and the opening of micro-cracks are modelled by a traction-separation relation. A heuristic approach is adopted to model the orientation of the cracks at the interfaces in the deformed configuration. A two-field formulation is derived, with the solid and the fluid velocities as unknowns. The weak formulation is derived next, assuming a Total Lagrangian formulation. This naturally leads to a set of coupled equations for the continuous and for the discontinuous parts of the mixture. The resulting discrete equations are nonlinear due to the cohesive-crack model, the large-deformation kinematic relations, and the coupling terms between the fine scale and the coarse scale. The capabilities of the model are shown at the hand of some example problems.

Keywords: Porous material, large deformation, crack propagation, partition of unity, cohesive zone model

1. Introduction

Since the work of Terzaghi [1] and Biot [2], fluid flow in a deforming porous medium has received considerable attention. Indeed, the subject is crucial for the understanding and the prediction of the physical behaviour of many systems of interest. Initially, research has focused on petroleum and geotechnical engineering [3]. More recently, the developed techniques have also been applied to biology and medical sciences. Studies have been carried out to understand the complexity of the structure as well as the physical processes in human soft tissues, e.g. blood perfusion [4], skin and subcutis [5] and cartilageous tissues including intervertebral discs [6].

Recently, a two-scale numerical model has been constructed for crack propagation in a deforming fluid-saturated porous medium subject to small strains [7, 8, 9]. The saturated porous material was modelled as a two-phase mixture, composed of a deforming solid skeleton and an interstitial fluid. Crack growth was initially modelled using linear-elastic fracture mechanics, but later also via a cohesive-zone approach, where the process zone is lumped into a single plane ahead of the crack tip. The opening of this plane is governed by a traction-separation relation. In order to allow for the nucleation and the propagation of cracks in arbitrary directions, irrespective of the structure of the underlying finite element mesh, the model exploits the partition-of-unity property of finite element shape functions [10], see also [11, 12, 13, 14]. At the fine scale the flow in the crack is modelled as a viscous fluid using Stokes' equations. Since the cross-sectional dimensions of the cavity formed by the crack are assumed to be small compared to its length, the flow equations can be averaged over the cross section of the cavity. The resulting equations provide the momentum and mass couplings to the standard equations for a porous material, which hold on the

*Corresponding author: René de Borst
Email addresses: F.Irzal@tue.nl (Faisal Irzal[1]), J.J.C.Remmers@tue.nl (Joris J. C. Remmers[1]), J.M.R.Huyghe@tue.nl (Jacques M. Huyghe[2]), Rene.DeBorst@glasgow.ac.uk (René de Borst[3])

coarse scale.

Soft tissues can experience large deformations. The small strain assumption then no longer holds. In this contribution, we therefore make the extension to a finite strain framework, introducing nonlinear kinematics in combination with a hyperelastic material response. Thus, we follow the motion of the solid skeleton using a Lagrangian description and express the momentum balance equations using this description. Subsequently, we write the mass balance equations identifying the spatial point as the instantaneous material point occupied by the solid phase. The resulting system of equations is nonlinear due to the cohesive-crack model, the geometrically nonlinear effect and presence of the coupling terms. A linearisation is applied to the system for use within a Newton-Raphson iterative procedure, and a weighted-time scheme is applied to discretise the system in the time domain.

The paper is ordered as follows. In the next section, the nonlinear kinematic relations for a fracturing porous material are elaborated. These relations are used to construct the linear momentum and mass balance relations in Section 3, complemented by constitutive relations for the mixture in the bulk as well as at the interface in Section 4. The spatial discretisation, which exploits the partition-of-unity property, is presented in Section 5, followed by implementation aspects in Section 6. The performance of the model is assessed in Section 7, followed by some concluding remarks.

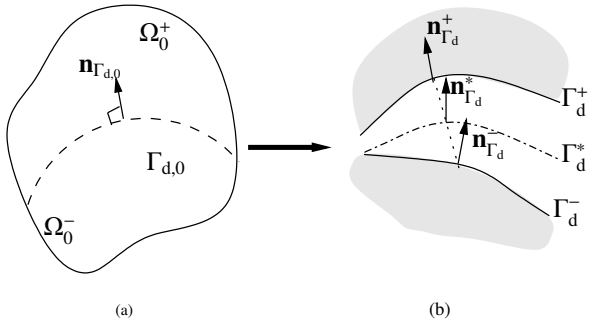

Figure 1: (a). Schematic representation of body Ω_0 crossed by a material discontinuity $\Gamma_{d,0}$ in the undeformed configuration. (b). Discontinuity interfaces Γ_d^+ and Γ_d^- and their normal vector representation in the deformed configuration

2. Nonlinear kinematics

Figure 1(a) shows a body crossed by a discontinuity $\Gamma_{d,0}$ in the reference or undeformed configuration. The body is divided by the discontinuity into two subdomains, Ω_0^+ and Ω_0^- ($\Omega_0 = \Omega_0^+ \cup \Omega_0^-$). A vector $\mathbf{n}_{\Gamma_{d,0}}$ is defined normal to the discontinuity surface $\Gamma_{d,0}$ in the direction of Ω_0^+. The total displacement field of the solid skeleton $\mathbf{u}$ consists of a continuous regular displacement field $\bar{\mathbf{u}}$ and a continuous additional displacement field $\hat{\mathbf{u}}$:

$$\mathbf{u}(\mathbf{X}, t) = \bar{\mathbf{u}}(\mathbf{X}, t) + \mathcal{H}_{\Gamma_{d,0}}\hat{\mathbf{u}}(\mathbf{X}, t), \tag{1}$$

where $\mathbf{X}$ is the position vector of a material point in the undeformed configuration and $\mathcal{H}_{\Gamma_{d,0}}$ is the Heaviside step function centered at the discontinuity and is defined as:

$$\mathcal{H}_{\Gamma_{d,0}}(\mathbf{X}) = \begin{cases} 1 & , \quad \mathbf{X} \in \Omega_0^+ \\ 0 & , \quad \mathbf{X} \in \Omega_0^-. \end{cases} \tag{2}$$

From the displacement decomposition in (1), the deformation map $\Phi(\mathbf{X}, t)$ for a body crossed by a discontinuity can be written as:

$$\begin{aligned} \Phi(\mathbf{X}, t) &:= \mathbf{x}(\mathbf{X}, t) \\ &= \mathbf{X} + \bar{\mathbf{u}}(\mathbf{X}, t) + \mathcal{H}_{\Gamma_{d,0}}\hat{\mathbf{u}}(\mathbf{X}, t), \end{aligned} \tag{3}$$

where $\mathbf{x}$ is the position vector of a material point in the deformed configuration. The velocity of the solid constituent is defined as

$$\dot{\mathbf{x}} = \frac{\mathrm{D}\mathbf{x}}{\mathrm{D}t} = \mathbf{v}_\mathrm{s} \tag{4}$$

where the superimposed dot indicates the material time derivative which follows the motion of the solid. The deformation gradient $\mathbf{F}$ is obtained by taking the gradient of (3) with respect to the undeformed configuration:

$$\mathbf{F} = \bar{\mathbf{F}} + \mathcal{H}_{\Gamma_{d,0}}\hat{\mathbf{F}}, \tag{5}$$

with $\bar{\mathbf{F}} = \mathbf{I} + \nabla_0\bar{\mathbf{u}}$ and $\hat{\mathbf{F}} = \nabla_0\hat{\mathbf{u}}$.

The volumetric change of the solid between the undeformed and deformed configuration is represented as $J = \det(\mathbf{F})$. Differentiation with respect to time yields

$$\dot{J} = J\,\nabla\mathbf{v}_\mathrm{s}. \tag{6}$$

The magnitude of the displacement jump $\mathbf{u}_\mathrm{d}$ at the discontinuity $\Gamma_{d,0}$ is represented as the magnitude of the additional displacement field $\hat{\mathbf{u}}$;

$$\mathbf{u}_\mathrm{d}(\mathbf{X}, t) = \hat{\mathbf{u}}(\mathbf{X}, t), \qquad \mathbf{X} \in \Gamma_{d,0}. \tag{7}$$

With aid of Nanson's relation for the normal $\mathbf{n}$ to a surface Γ

$$\mathbf{n} = J\,\mathbf{F}^{-\mathrm{T}}\mathbf{n}_0\frac{\mathrm{d}\Gamma_0}{\mathrm{d}\Gamma}, \tag{8}$$

the expressions for the normals at the Ω_0^- side and at the

Ω_0^+ side of the interface can be derived as

$$\mathbf{n}_{\Gamma_\mathrm{d}}^- = \det(\bar{\mathbf{F}})\,\bar{\mathbf{F}}^{-\mathrm{T}}\mathbf{n}_{\mathrm{d},0}\frac{\mathrm{d}\Gamma_{\mathrm{d},0}}{\mathrm{d}\Gamma_\mathrm{d}^-} \tag{9}$$

$$\mathbf{n}_{\Gamma_\mathrm{d}}^+ = \det(\bar{\mathbf{F}}+\hat{\mathbf{F}})\left(\bar{\mathbf{F}}+\hat{\mathbf{F}}\right)^{-\mathrm{T}}\mathbf{n}_{\mathrm{d},0}\frac{\mathrm{d}\Gamma_{\mathrm{d},0}}{\mathrm{d}\Gamma_\mathrm{d}^+}, \tag{10}$$

respectively. Figure 1(b) illustrates the normal vector at the discontinuities. Considering the fact that the magnitude of the opening $\mathbf{u}_\mathrm{d}$ will be relatively small, it is assumed that an average normal can be defined for use within a cohesive-zone model [13]:

$$\mathbf{n}_{\Gamma_\mathrm{d}}^* = \det\left(\bar{\mathbf{F}}+\frac{1}{2}\hat{\mathbf{F}}\right)\left(\bar{\mathbf{F}}+\frac{1}{2}\hat{\mathbf{F}}\right)^{-1}\mathbf{n}_{\mathrm{d},0}\frac{\mathrm{d}\Gamma_{\mathrm{d},0}}{\mathrm{d}\Gamma_\mathrm{d}^*}. \tag{11}$$

The vector $\mathbf{n}_{\Gamma_\mathrm{d}}^*$ is used to define the traction vector at the 'average' discontinuity plane Γ_d^*, and to resolve a displacement jump into normal and tangential components. To simplify the notation, $\mathbf{n}_{\Gamma_\mathrm{d}}$ will henceforth substitute $\mathbf{n}_{\Gamma_\mathrm{d}}^*$.

3. Balance equations

We consider a mixture that consists of a solid skeleton with an interstitial fluid. Furthermore, it is assumed that there is no mass transfer between the constituents. The inertia effects, convective term and gravity acceleration can be neglected and the process is considered as isothermal. With these assumptions we write the balance of linear momentum for the solid and the fluid phases as:

$$\nabla\cdot\boldsymbol{\sigma}_\pi + \hat{\mathbf{p}}_\pi = \mathbf{0}, \tag{12}$$

where $\boldsymbol{\sigma}_\pi$ denotes the stress tensor of constituent π. In the remainder we will adopt $\pi = \mathrm{s},\mathrm{f}$, with s and f denoting the solid and fluid phases, respectively. Furthermore, $\hat{\mathbf{p}}_\pi$ is the source of momentum for constituent π from the other constituent, which takes into account the possible local drag interaction between solid and fluid. Considering that the latter source terms satisfy the momentum production constraint

$$\sum_{\pi=s,f}\hat{\mathbf{p}}_\pi = \mathbf{0}, \tag{13}$$

and adding the momentum balances for the solid and the fluid parts of the mixture, we obtain the balance of linear momentum for the mixture in the current, or deformed, configuration as:

$$\nabla\cdot\boldsymbol{\sigma} = \mathbf{0}, \tag{14}$$

where the stress is composed of a solid and a fluid part:

$$\boldsymbol{\sigma} = \boldsymbol{\sigma}_\mathrm{s} + \boldsymbol{\sigma}_\mathrm{f}. \tag{15}$$

Now, defining the corresponding first Piola-Kirchhoff partial stress tensor as $\mathbf{P}_\pi = J\,\mathbf{F}^{-1}\cdot\boldsymbol{\sigma}_\pi$, the total first Piola-Kirchhoff stress tensor is given by

$$\mathbf{P} = \mathbf{P}_\mathrm{s} + \mathbf{P}_\mathrm{f}. \tag{16}$$

and the Lagrangian formulation of the linear momentum equation (14) takes the form

$$\nabla_0\cdot\mathbf{P} = \mathbf{0}. \tag{17}$$

Under the same assumptions, the local mass balance of the constituent π reads

$$\frac{\partial\rho_\pi}{\partial t} + \rho_\pi\nabla\cdot\mathbf{v}_\pi = 0 \tag{18}$$

where ρ_π denotes the apparent density and $\mathbf{v}_\pi$ is the absolute velocity of constituent π. The mass balance equations of the (moving) constituents are rewritten in terms of the material time derivative following the motion of the solid constituent [15]:

$$\dot{m}_\mathrm{s} = 0 \quad\text{and}\quad \dot{m}_\mathrm{f} + J\,\nabla\cdot\mathbf{q} = 0 \tag{19}$$

where the Lagrange apparent density m_π represents the mass of constituent π currently contained in the mixture volume that was initially equal to unity

$$m_\pi = J\,\rho_\pi. \tag{20}$$

$\mathbf{q}$ is the relative mass flow of the fluid phase with respect to the solid matrix, given by relation:

$$\mathbf{q} = \rho_\mathrm{f}\left(\mathbf{v}_\mathrm{f} - \mathbf{v}_\mathrm{s}\right). \tag{21}$$

The volumetric response of the pore fluid can be written as [16]

$$p = M(-\alpha\varepsilon + m_\mathrm{f}), \tag{22}$$

where ε represents the volumetric strain of the solid matrix,

$$\varepsilon = J - 1, \tag{23}$$

α is the Biot coefficient, and M denotes the compressibility modulus, defined through

$$\frac{1}{M} = \frac{\phi}{K_f} + \frac{1-\phi}{K_s}, \tag{24}$$

where the coefficients K_s , K_f and ϕ represent the compressibility of the solid part, the compressibility of the

fluid part, and the porosity of the medium, respectively.

Taking the material time derivative of expression (22), summing both constituents, and using equations (19) and (23), the mass balance of the total mixture is obtained as:

$$\frac{1}{M}\dot{p} + \alpha\dot{J} + \nabla \cdot \mathbf{q} = 0, \tag{25}$$

Pulling back to the undeformed configuration results in:

$$\frac{1}{M}\dot{p} + \alpha\dot{J} + \nabla_0 \cdot \mathbf{Q} = 0, \tag{26}$$

where

$$\mathbf{Q} = J\,\mathbf{F}^{-1} \cdot \mathbf{q} \tag{27}$$

is the Piola transform of $\mathbf{q}$ into the undeformed configuration.

The balance of momentum of the saturated medium, equation (14) is complemented by the boundary conditions

$$\mathbf{n}_\Gamma \cdot \boldsymbol{\sigma} = \mathbf{t}_p, \qquad \mathbf{v} = \bar{\mathbf{v}}, \tag{28}$$

which hold on complementary parts of the boundary Γ_t and Γ_v, with $\Gamma = \Gamma_t \cup \Gamma_v$, $\Gamma_t \cap \Gamma_v = \emptyset$, $\mathbf{t}_p$ and $\bar{\mathbf{v}}$ are the prescribed external traction and the prescribed velocity, respectively. The balance of mass, equation (18), is complemented by the boundary conditions

$$\mathbf{n}_\Gamma \cdot \mathbf{q} = q_p, \qquad p = \bar{p}, \tag{29}$$

which hold on complementary parts of the boundary Γ_q and Γ_p, with $\Gamma = \Gamma_q \cup \Gamma_p$, $\Gamma_q \cap \Gamma_p = \emptyset$, q_p and $\bar{p}$ being the prescribed amount of outflow of pore fluid and the prescribed pressure, respectively. Figure (2) shows a body Ω crossed by a material discontinuity with the aforementioned boundary conditions.

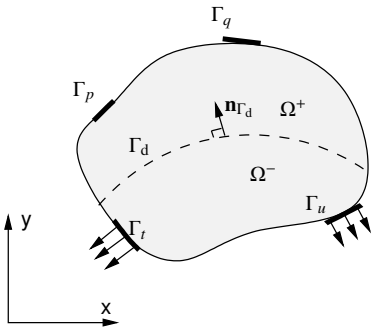

Figure 2: Body Ω crossed by a discontinuity Γ_d and complemented by boundary conditions. The x, y coordinate system represents the global coordinate system of the body.

4. Constitutive equations and couplings

To close the mathematical problem, constitutive relations for the mechanical deformation of the solid skeleton and the interstitial fluid must be specified.

4.1. Models for the bulk

The effective stress rate in the solid skeleton, $\dot{\boldsymbol{\sigma}}_e$ is related to the strain rate $\dot{\boldsymbol{\varepsilon}}$ by a linear stress-strain relation for the solid

$$\dot{\boldsymbol{\sigma}}_e = \mathbf{D} : \dot{\boldsymbol{\varepsilon}} \tag{30}$$

where $\mathbf{D}$ is the fourth-order tangent stiffness tensor of the solid material. In the examples, a Neo-Hookean type of material behaviour will be applied. This model can be regarded as a simple extension of the isotropic-linear law to large deformations.

For the flow of the pore fluid, we assume that Darcy's relation holds for isotropic media [2]

$$\mathbf{q} = -\frac{\mathbf{k}}{\mu}\,\nabla p, \tag{31}$$

where $\mathbf{k}$ is the intrinsic permeability tensor of the porous material and μ is the dynamic viscosity of the interstitial fluid. In a Lagrangian framework it reads

$$\mathbf{Q} = -\frac{\mathbf{K}}{\mu}\,\nabla_0 p, \tag{32}$$

where

$$\mathbf{K} = J\,\mathbf{F}^{-1} \cdot \mathbf{k} \cdot \mathbf{F}^{-\mathrm{T}} \tag{33}$$

is the pull-back intrinsic permeability tensor relating the fluid relative velocity vector $\mathbf{q}$ from the deformed to the undeformed configuration of the solid matrix.

4.2. Interface behaviour

The constitutive law at the interface is taken to be a phenomenological mechanical relation between the traction and the displacement jump across the surface, namely

$$\mathbf{t}_d = \mathbf{t}_d(\mathbf{u}_d, \kappa) \tag{34}$$

with κ a history parameter. The behaviour that needs to be captured is that at first, the magnitude of the traction increases, reaches a maximum, and then approaches zero with increasing separation. To this end, we use the traction-separation law proposed by Xu and Needleman [17], which allows for tangential as well as normal decohesion.

After linearisation in an incremental-iterative solution procedure, one obtains

$$\dot{\mathbf{t}}_d = \mathbf{T}\,\dot{\mathbf{u}}_d, \tag{35}$$

with $\mathbf{T}$ the material tangent stiffness matrix of the discrete traction-separation law:

$$\mathbf{T} = \frac{\partial \mathbf{t}_\mathrm{d}}{\partial \mathbf{u}_\mathrm{d}} + \frac{\partial \mathbf{t}_\mathrm{d}}{\partial \kappa} \frac{\partial \kappa}{\partial \mathbf{u}_\mathrm{d}}. \tag{36}$$

The traction from the solid part at the interface is coupled to the pressure of the fluid. Assuming stress continuity from the cavity to the bulk, we have:

$$\mathbf{n}_{\Gamma_\mathrm{d}} \cdot \mathbf{P} = \mathbf{t}_\mathrm{d} - p\mathbf{n}_{\Gamma_\mathrm{d}}. \tag{37}$$

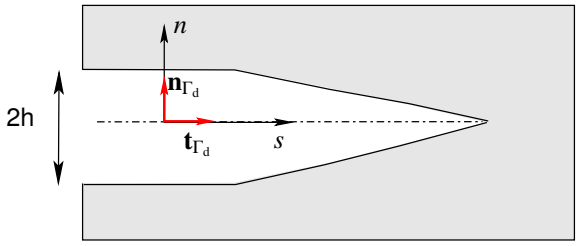

Figure 3: Geometry and local coordinate system in cavity in the deformed configuration.

To arrive at a relation for the leakage flux of the pore fluids into the vicinity of the crack, the flow continuity equation for the fluid inside the crack is averaged over the cross section. The results obtained are included in the mass transfer coupling terms that emerge in the weak form of the continuity equations of flow in the porous medium. The continuity equation for the fluid flow in the crack is identical to that of the surrounding porous medium. In what follows, the formulations are presented in the current local Cartesian coordinate (s, n) with directions aligned with the tangent and normal unit vectors to the discontinuity, $\mathbf{t}_{\Gamma_\mathrm{d}}$ and $\mathbf{n}_{\Gamma_\mathrm{d}}$, respectively. Effectively, one has, cf. equation (25):

$$\int_{-h}^{h} \left(\frac{1}{M} \dot{p} + \alpha \nabla \cdot \mathbf{v}_\mathrm{s} + \nabla \cdot \mathbf{q} \right) \mathrm{d}n = 0. \tag{38}$$

Since the cross section of the cavity is relatively small to its length, the variation of the fluid pressure across the discontinuity is ignored. Hence, the first term of equation (38) can be rewritten as

$$\int_{-h}^{h} \frac{1}{M} \dot{p} \, \mathrm{d}n = \frac{2h}{M} \dot{p} \, . \tag{39}$$

Using the definition of the divergence in the local coordinate system and making restriction to a two-dimensional configuration for brevity, the following expression for the second term of Equation (38) is obtained:

$$\int_{-h}^{h} \alpha \nabla \cdot \mathbf{v}_\mathrm{s} \, \mathrm{d}n = \int_{-h}^{h} \alpha \left(\frac{\partial v}{\partial s} + \frac{\partial w}{\partial n} \right) \mathrm{d}n \tag{40}$$

where v and w denote the tangential and normal components of the solid velocity, respectively. Because h is small compared to the other dimensions, it can be assumed that the tangential component of the solid velocity varies linearly with n. Consequently, the derivative with respect to s also varies linearly with n. Taking this into account, the contribution which includes the tangential derivative can be integrated analytically. Defining $\langle \cdot \rangle = (\cdot^+ + \cdot^-)/2$ as the average of the corresponding values at the discontinuity faces, one obtains the following relation

$$\begin{aligned} \int_{-h}^{h} \alpha \nabla \cdot \mathbf{v}_\mathrm{s} \, \mathrm{d}n &= 2h\alpha \frac{1}{2} \left(\frac{\partial v}{\partial s}(h) + \frac{\partial v}{\partial s}(-h) \right) \\ &\quad + \alpha \left(w(h) - w(-h) \right) \\ &= 2h\alpha \langle \frac{\partial v}{\partial s} \rangle + \alpha [\![w]\!], \end{aligned} \tag{41}$$

where the difference in the normal velocity between both crack faces $[\![w]\!]$ is given by

$$[\![w]\!] = 2\dot{h}. \tag{42}$$

Taking into account the divergence operator in the local coordinate system and assuming that relative fluid velocity in tangential direction with respect to the crack, the following expression is obtained for the third term of equation (38)

$$\begin{aligned} \int_{-h}^{h} \nabla \cdot \mathbf{q} \, \mathrm{d}n &= \int_{-h}^{h} \left(\frac{\partial q_s}{\partial s} + \frac{\partial q_n}{\partial n} \right) \mathrm{d}n \\ &= \int_{-h}^{h} \frac{\partial}{\partial s} \left(-k_d \frac{\partial p}{\partial s} \right) \mathrm{d}n + \int_{-h}^{h} \frac{\partial q_n}{\partial n} \mathrm{d}n \end{aligned} \tag{43}$$

where k_d is the permeability in the discontinuity, and q_s and q_n denote the tangential and normal components of the relative fluid velocity, respectively. Since the fluid pressure is assumed to be uniform across the discontinuity, the first and the second derivatives with respect to the s-axis are constant along n. Hence,

$$\int_{-h}^{h} \nabla \cdot \mathbf{q} \, \mathrm{d}n = 2h \frac{\partial}{\partial s} \left(-k_d \frac{\partial p}{\partial s} \right) + [\![q_n]\!]. \tag{44}$$

The normal component $[\![q_n]\!] = \mathbf{n}_{\Gamma_\mathrm{d}} \cdot \mathbf{q}_\mathrm{d}$ is the term sought after. Hence, by substituting the components of equation (38) and rearranging, the micro-flow coupling term

is obtained:

$$\mathbf{n}_{\Gamma_\mathrm{d}} \cdot \mathbf{q}_\mathrm{d} = 2h\frac{\partial}{\partial s}\left(k_d \frac{\partial p}{\partial s}\right) - \frac{2h}{M}\dot{p} - 2h\alpha\langle\frac{\partial v}{\partial s}\rangle - 2\alpha\dot{h}. \quad (45)$$

5. Weak forms and numerical elaboration

The weak forms for the momentum balance and the mass balance in the undeformed configuration are expressed as:

$$\int_{\Omega_0} \nabla_0\boldsymbol{\eta} : \mathbf{P}\,\mathrm{d}\Omega_0 + \int_{\Gamma_{\mathrm{d},0}} [\![\boldsymbol{\eta}]\!] \cdot \mathbf{n}_{\Gamma_{\mathrm{d},0}} \cdot \mathbf{P}\,\mathrm{d}\Gamma_0 = \int_{\Gamma_{t,0}} \boldsymbol{\eta} \cdot \mathbf{t}_0\,\mathrm{d}\Gamma_0 \quad (46)$$

and

$$-\int_{\Omega_0} \alpha\,\dot{J}\,\zeta\,\mathrm{d}\Omega_0 + \int_{\Omega_0} \nabla_0\zeta\,\frac{\mathbf{K}}{\mu}\,\nabla_0 p\,\mathrm{d}\Omega_0 - \int_{\Omega_0} \zeta\,J\,M^{-1}\dot{p}\,\mathrm{d}\Omega_0 + \int_{\Gamma_{\mathrm{d},0}} [\![\zeta]\!]\,(\mathbf{n}_{\Gamma_{\mathrm{d},0}} \cdot \mathbf{q}_\mathrm{d})\,\mathrm{d}\Gamma_0 = \int_{\Gamma_q} \zeta\,\mathbf{n}_0 \cdot \mathbf{q}_0\,\mathrm{d}\Gamma_0, \quad (47)$$

where $\mathbf{t}_0$ and $\mathbf{q}_0$ are the nominal traction and the prescribed outflow fluid acting on $\Gamma_{t,0}$ and $\Gamma_{p,0}$, respectively, while $\boldsymbol{\eta}$ and ζ are admissible test functions for the displacement and the pressure, respectively. The term $[\![\cdot]\!]$ describes the discontinuous part of the system of equation and is calculated in the deformed configuration.

5.1. Discretisation

The model presented in the previous sections imposes some restrictions on the assumed displacement and the pressure fields. The opening of the discontinuity must be described with sufficient accuracy in order to reproduce the cavity geometry properly. These requirements can be satisfied exploiting the partition-of-unity property of finite element shape functions [10].

In the spirit of previous works on crack propagation in a single-phase medium [11, 12, 13, 14] the interpolation of each component of the displacement field of the solid phase is enriched by discontinuous functions:

$$u_s = \sum_{I\in\mathcal{N}} N_I \bar{u}_I + \sum_{I\in\mathcal{N}_{sup}} N_I \hat{u}_I, \quad (48)$$

where N_I are the standard finite element shape functions supported by the set of nodes $\mathcal{N}$ included in the discretised domain Ω. Nodes in $\mathcal{N}_{sup}$ have their support completely cut by the discontinuity, as depicted in Figure (4). They hold additional degrees of freedom $\hat{u}_I$ corresponding to the discontinuous function $\mathcal{H}_{\Gamma_{\mathrm{d},0}}$.

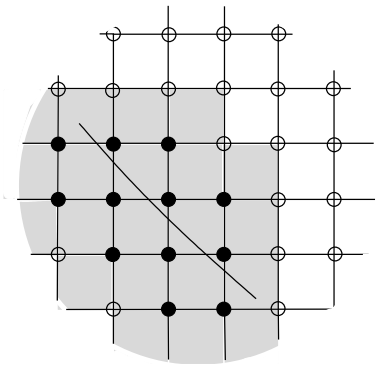

Figure 4: Two-dimensional finite element mesh with a discontinuity denoted by the bold line. Nodes with enhanced degrees of freedom are indicated by solid dots. The grey elements contain additional terms in the stiffness matrix and the internal force vector.

Symbolically, Equation (48) can be written as

$$\mathbf{u}_\mathrm{s} = \mathbf{N}\,\underline{\mathbf{u}} \quad (49)$$

where $\mathbf{N}$ is a matrix that contains the standard interpolation polynomials N_I as well as the discontinuous function $\mathcal{H}_{\Gamma_\mathrm{d}}$, and the array $\underline{\mathbf{u}}$ contains the displacement degrees of freedom $\bar{u}_I$ and $\hat{u}_I$. Furthermore, we define the matrix $[\![\mathbf{N}]\!]$ which contains the jumps in the interpolation polynomials, and the matrix $\mathbf{B}_0$ with the components

$$[\mathbf{B}_0]_{ijkI} = \mathrm{sym}_{(i,j)}\left(\frac{\partial N_I}{\partial X_i} F_{kj}\right), \quad (50)$$

which contains the bounded part of spatial derivatives of $\mathbf{N}$ with respect to the undeformed configuration. The deformation gradient F_{kj} is written in Voigt notation [18].

For the approximation of the pressure, the standard finite element interpolation is enriched by the distance function $\mathcal{D}_{\Gamma_{\mathrm{d},0}}$, where

$$\mathbf{n}_{\Gamma_{\mathrm{d},0}} \cdot \mathcal{D}_{\Gamma_{\mathrm{d},0}} = \mathcal{H}_{\Gamma_{\mathrm{d},0}} \quad (51)$$

All nodes whose support is cut by the discontinuity $\mathcal{N}_{sup}$, also hold additional pressure degree of freedom

$$p = \sum_{I\in\mathcal{N}} H_I \bar{p}_I + \sum_{I\in\mathcal{N}_{sup}} H_I \mathcal{D}_{\Gamma_{\mathrm{d},0}} \hat{p}_I, \quad (52)$$

where H_I are the finite element shape functions used for pressure field interpolation. In a similar fashion to the displacement interpolation, one writes Equation (52)

symbolically as

$$p = \mathbf{H}\,\underline{\mathbf{p}} \tag{53}$$

where $\mathbf{H}$ contains the standard interpolation polynomials H_I as well as the discontinuous enrichment function $\mathcal{D}_{\Gamma_{\mathrm{d},0}}$, and the array $\underline{\mathbf{p}}$ contains the pressure degrees of freedom $\bar{p}_I$ and $\hat{p}_I$.

The choice for N_I and H_I is driven by modelling requirements. Indeed, the modelling of the fluid flow inside the cavity requires the second derivative of the pressure as seen from equation (45). Hence, the order of the finite element shape function H_I has to be sufficiently high, otherwise the coupling between the fluid flow in the cavity and the bulk part will be lost. Furthermore, the order of the finite element shape function N_I must be greater than or equal to the order of H_I for consistency in the discrete balance of momentum, so that spurious oscillations or locking in the pressure field are avoided [19]. However, we will use a quadrilateral element with bilinear shape functions for the displacement and for the pressure fields for simplicity.

5.2. Discrete equations and resolution

Adopting a Bubnov-Galerkin formulation, the variations of the displacement and the pressure are interpolated in the same manner. Hence, inserting the discretised variations of displacements and pressures into the weak forms as described in equations (46) and (47) yields the discretised version of the equilibrium equations for all admissible variations of displacement and pressure. This gives:

$$\int_{V_0} \mathbf{B}_0^{\mathrm{T}}\,\mathbf{P}\,\mathrm{d}V_0 + \mathbf{f}_{\mathrm{int}} = \mathbf{f}_{\mathrm{ext}} \tag{54}$$

$$-\int_{V_0} \alpha\,\dot{J}\,\mathbf{H}^{\mathrm{T}}\,\mathrm{d}V_0 + \int_{V_0} \nabla_0\mathbf{H}^{\mathrm{T}}\,\frac{\mathbf{K}}{\mu}\nabla_0 p\,\mathrm{d}V_0 - \int_{V_0} J\,M^{-1}\mathbf{H}^{\mathrm{T}}\dot{p}\,\mathrm{d}V_0 + \mathbf{q}_{\mathrm{int}} = \mathbf{q}_{\mathrm{ext}} \tag{55}$$

The external force and flux vectors are given by:

$$\mathbf{f}_{\mathrm{ext}} = \int_{S_t} \mathbf{N}^{\mathrm{T}}\mathbf{t}_0\,\mathrm{d}S_0, \tag{56}$$

$$\mathbf{q}_{\mathrm{ext}} = \int_{S_q} \mathbf{H}^{\mathrm{T}}\mathbf{n}_{\Gamma_0}^{\mathrm{T}}\mathbf{q}_0\,\mathrm{d}S_0. \tag{57}$$

The interfacial force vector $\mathbf{f}_{\mathrm{int}}$ is discretised from (54) to give:

$$\mathbf{f}_{\mathrm{int}} = \int_{S_d} \mathbf{N}^{\mathrm{T}}\mathbf{t}_{\mathrm{d}}\,\mathrm{d}S_0 - \int_{S_d} \mathbf{N}^{\mathrm{T}}\mathbf{n}_{\Gamma_{\mathrm{d}}}\,p\,\mathrm{d}S_0 \tag{58}$$

The interfacial flux vector can be derived in a similar fashion to give:

$$\mathbf{q}_{\mathrm{int}} = \int_{S_d} \mathbf{H}^{\mathrm{T}}\mathbf{n}_{\Gamma_{\mathrm{d}}}^{\mathrm{T}}\mathbf{q}_{\mathrm{d}}\,\mathrm{d}S_0. \tag{59}$$

The interfacial flux vector $\mathbf{q}_{\mathrm{int}}$ can subsequently be elaborated by incorporating the discrete form of (45), cf. Reference [9].

The time integration is carried out using a weighted-time scheme, where the differential terms are approximated linearly by considering the residual values between the current and the previous step, and the values of the independent variables are weighted results of the current and previous step:

$$\left(\frac{\mathrm{d}\mathbf{Z}}{\mathrm{d}t}\right)_{n+\theta} = \frac{\mathbf{Z}_{n+1} - \mathbf{Z}_n}{\Delta t}$$
$$\mathbf{Z}_{n+\theta} = \theta\mathbf{Z}_{n+1} + (1-\theta)\mathbf{Z}_n \tag{60}$$

where $\mathbf{Z} = \{\underline{\mathbf{u}}\,,\underline{\mathbf{p}}\}^{\mathrm{T}}$, Δt gives the time increment, $\mathbf{Z}_n$ and $\mathbf{Z}_{n+1}$ are the state vectors at times t_n and t_{n+1}, while θ is a parameter bounded by the interval $[0, 1]$. The system of equations of (54) and (55) is evaluated at time $t_{n+\theta}$. A Crank-Nicholson scheme is retrieved for $\theta = \frac{1}{2}$, which is unconditionally stable for $\theta > \frac{1}{2}$ [20]. In the remainder we will use the backward scheme $\theta = 1$.

A Newton-Raphson procedure is used to compute the solution at each time step. For this purpose a residual vector $\mathbf{R}^i$ is defined at iteration i as

$$\mathbf{R}^i = \begin{bmatrix} \mathbf{0} & \mathbf{0} \\ \mathbf{K}_{up}^{\mathrm{T}} & \mathbf{K}_{pp}^{(1)} \end{bmatrix}\begin{pmatrix} \Delta\underline{\mathbf{u}} \\ \Delta\underline{\mathbf{p}} \end{pmatrix}^i + \begin{bmatrix} \mathbf{K}_{uu} & \mathbf{K}_{up} \\ \mathbf{0} & \Delta t\mathbf{K}_{pp}^{(2)} \end{bmatrix}\begin{pmatrix} \underline{\mathbf{u}} \\ \underline{\mathbf{p}} \end{pmatrix}^i + \begin{pmatrix} \mathbf{f}_{\mathrm{int}} \\ \Delta t\mathbf{q}_{\mathrm{int}} \end{pmatrix}^i - \begin{pmatrix} \mathbf{f}_{\mathrm{ext}} \\ \Delta t\mathbf{q}_{\mathrm{ext}} \end{pmatrix}^i \tag{61}$$

where the stiffness matrices are defined as

$$\mathbf{K}_{uu} = \int_{V_0} \mathbf{B}_0^{\mathrm{T}}\mathbf{D}\mathbf{B}_0\,\mathrm{d}V_0 + \int_{V_0} \boldsymbol{\mathcal{B}}_0^{\mathrm{T}}\mathbf{P}\boldsymbol{\mathcal{B}}_0\,\mathrm{d}V_0 \tag{62}$$

$$\mathbf{K}_{up} = -\int_{V_0} \alpha\mathbf{B}_0^{\mathrm{T}}\mathbf{m}\mathbf{H}\,\mathrm{d}V_0 \tag{63}$$

$$\mathbf{K}_{pp}^{(1)} = -\int_{V_0} M^{-1}\mathbf{H}^{\mathrm{T}}\mathbf{H}\,\mathrm{d}V_0 \tag{64}$$

$$\mathbf{K}_{pp}^{(2)} = -\int_{V_0} \nabla_0\mathbf{H}^{\mathrm{T}}\,\frac{\mathbf{K}}{\mu}\,\nabla_0\mathbf{H}\mathrm{d}V_0 \tag{65}$$

where

$$\boldsymbol{\mathcal{B}}_0^{\mathrm{T}} = \begin{bmatrix} \dfrac{\partial N_I}{\partial X_1}\mathbf{I} & \dfrac{\partial N_I}{\partial X_2}\mathbf{I} & \dfrac{\partial N_I}{\partial X_3}\mathbf{I} \end{bmatrix}, \tag{66}$$

and $\mathbf{I}$ is the identity matrix. The stiffness matrix $\mathbf{K}_{uu}$

consists of the material contribution and the geometric contribution of the stiffness. The matrix coupling term between solid and fluid is denoted by $\mathbf{K}_{up}$. In a full Newton-Raphson algorithm, the iterative matrix $\mathbf{K}^i$ is the Jacobian matrix of the residual $\mathbf{R}$:

$$\mathbf{K}^i = \begin{bmatrix} \mathbf{K}_{uu} + \dfrac{\partial \mathbf{f}_{\text{int}}}{\partial \underline{\mathbf{u}}} & \mathbf{K}_{up} + \dfrac{\partial \mathbf{f}_{\text{int}}}{\partial \underline{\mathbf{p}}} \\ \mathbf{K}_{up}^{\mathrm{T}} + \Delta t \dfrac{\partial \mathbf{q}_{\text{int}}}{\partial \underline{\mathbf{u}}} & \mathbf{K}_{pp}^{(1)} + \Delta t \theta \mathbf{K}_{pp}^{(2)} + \Delta t \dfrac{\partial \mathbf{q}_{\text{int}}}{\partial \underline{\mathbf{p}}} \end{bmatrix}. \tag{67}$$

When an element is supported by one or more enriched nodes, the stiffness matrix and force vector will have additional terms. The additional terms at the interface, i.e, the cohesive traction (37) and the mass coupling terms (45) cause the resulting stiffness matrix to become nonsymmetric. The linearisation of the additional terms with respect to the geometric contribution also generates a nonsymmetric contribution, but this plays a significant role only when a discontinuity at which tractions are acting undergoes large rotations or significant changes in area [13]. Enforcing symmetry normally slightly decreases the convergence rate [13], but allows an easier implementation and less multiplications per iteration. In this paper, the computations have been carried out with the following stiffness matrix:

$$\mathbf{K}^i = \begin{bmatrix} \mathbf{K}_{uu} + \dfrac{\partial \mathbf{f}_{\text{int}}}{\partial \underline{\mathbf{u}}} & \mathbf{K}_{up} \\ \mathbf{K}_{up}^{\mathrm{T}} & \mathbf{K}_{pp}^{(1)} + \Delta t \theta \mathbf{K}_{pp}^{(2)} \end{bmatrix}. \tag{68}$$

6. Finite element implementation

The finite element implementation of the model follows largely that presented in reference [7]. For completeness, some details of the implementation are reviewed, particularly with respect to the resulting stiffness matrix of the system, which consist of a material part, a geometric part and coupling terms.

The key step in the finite element implementation is the selection of nodes where extra enhanced degree of freedom should be added. We consider the specimen with a static interface shown in Figure 4. In the finite element model, the interface is modelled as a discontinuity in a structured mesh composed of four-noded elements. Additional degrees of freedom are added to nodes whose support is crossed by a discontinuity. The other nodes remain unchanged. Since only the nodes of elements that are crossed by the discontinuity have additional degrees of freedom, the total number of degrees of freedom of the system is slightly larger than for the case without a discontinuity.

From the computational aspect, an important issue is the numerical integration of the continuum element in the presence of a discontinuity as well as the numerical integration of the coupling terms at a discontinuty. For this purpose, standard Gauss integration is applied for the continuum elements crossed by a discontinuity. To integrate the traction forces and leakage flux at a discontinuity, integration points located at the discontinuity are used. To achieve an accurate numerical integration, one needs sufficient integration points on each side of an element crossed by a discontinuity [11]. Details of the adopted integration scheme can be found in [12].

To simulate a propagating crack a criterion is needed that governs the crack evolution. For given load level, the equivalent traction at the Gauss points in the element ahead of the crack tip is checked against the cohesive strength of the material t_c. If the equivalent traction at any of the Gauss points in the element ahead of the crack tip exceeds the cohesive strength, the crack is extended into that element until it touches one of the element edges. The equivalent traction t_{eq} is computed from the tractions of an averaged effective stress tensor at the crack tip [21]:

$$t_{eq}(\theta) = \sqrt{t_n^2 + t_s^2/\beta} \tag{69}$$

where

$$t_n = \mathbf{n}^{\mathrm{T}} \boldsymbol{\sigma}_{\mathrm{e}} \mathbf{n}, \quad t_s = \mathbf{s}^{\mathrm{T}} \boldsymbol{\sigma}_{\mathrm{e}} \mathbf{n}, \tag{70}$$

represent the normal and shear tractions, respectively, which lie along an imaginary axis which constructs an angle θ with respect to x-axis. The parameter β defines the ratio between the shear and the normal strength of the material.

Since the stress field varies strongly in the vicinity of the crack tip, the local stress field is not reliable for the prediction of the crack growth direction. Following Wells and Sluys [12] we use a smoothing of the stresses around the tip and use the following stress measure in the criterion for crack propagation:

$$\boldsymbol{\sigma}_{\mathrm{e}}^{tip} = \frac{\int_\Omega w \, \boldsymbol{\sigma}_{\mathrm{e}} \mathrm{d}\Omega}{\int_\Omega w \, \mathrm{d}\Omega}, \tag{71}$$

in which w is the Gaussian weight function that smoothens the stress field at the tip neighborhood defined as

$$w = \frac{1}{(2\pi)^{3/2} l^3} \exp\left(-\frac{r^2}{2l}\right), \tag{72}$$

with r the distance to the tip and l a characteristic length which defines the size of region of influence of the

Name	Symbol	Value
Young's modulus	E	25.85 GPa
Poisson's ratio	ν	0.18
Solid bulk modulus	K_s	13.46 GPa
Fluid bulk modulus	K_f	0.2 GPa
Intrinsic permeability	k	2.78e-10 mm^2
Biot's coefficient	α	1
Porosity	ϕ	0.2
Fluid dynamic viscosity	μ	1.0e-9 MPa s
Cohesive strength	t_c	2.7 MPa
Fracture toughness	G_c	0.095 N/mm

Table 1: Material properties for example problems

stress, which is often taken as approximately three times the typical element size [12].

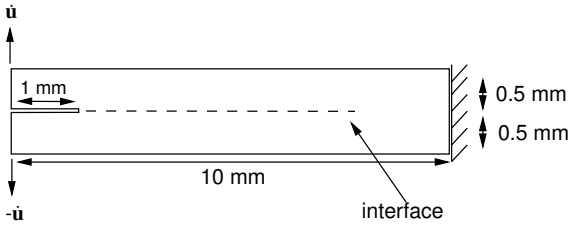

Figure 5: Peel test geometry for two layer porous material. A 1 mm crack is initiated with the dashed line represent the given crack propagation.

7. Examples

The numerical examples in this section illustrate the performance of the model. All examples are two-dimensional, with the quadrilateral element used as the underlying element with bilinear shape function for the displacements and the pressure. Neo-Hookean material behaviour is assumed to model the material in the large-strain regime. The material properties are summarised in Table 1.

7.1. Peel test

To test the geometrically nonlinear model, a slender beam composed of a fluid-saturated porous material, shown in Figure 5, is analysed. A 1 mm pre-notch is located at the symmetry axis of the beam. The beam is clamped on the right-hand side, and a vertical velocity $v = 10^{-2}$ mm/s is applied to the top left and the bottom left corner nodes of the beam. All boundaries of the beam are assumed to be impervious and the micro-flow coupling is not yet taken into account in this example.

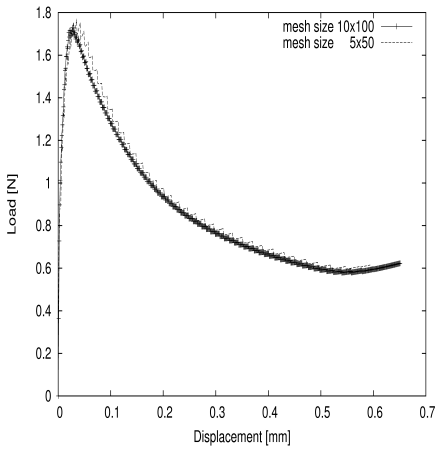

Figure 6: Load-displacement diagram for peel test

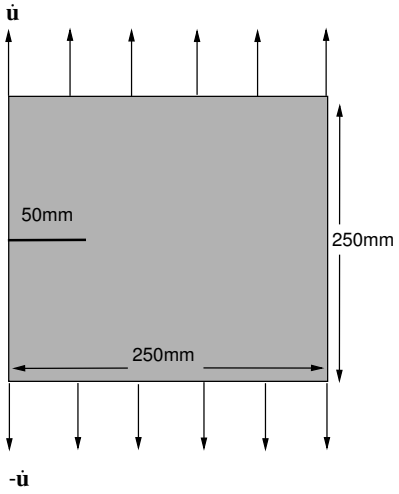

Figure 7: Delamination test geometry for two square plate porous material with a 50 mm crack notch.

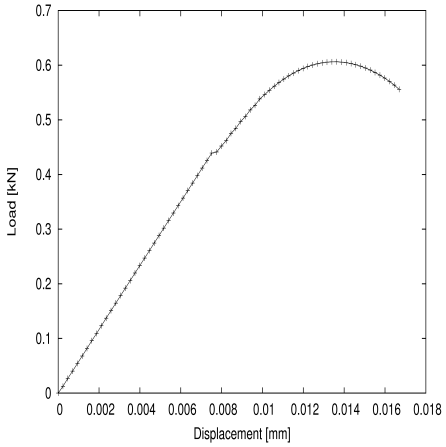

Figure 8: Load-displacement diagram for delamination test

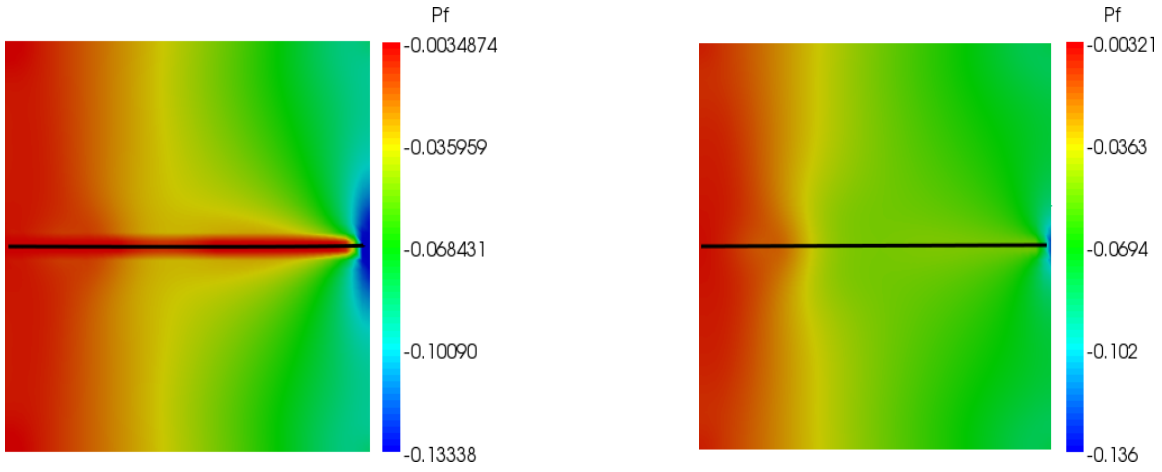

(a) (b)

Figure 9: Fluid pressure profiles [MPa]: (a) with micro-flow coupling and (b) without micro-flow coupling

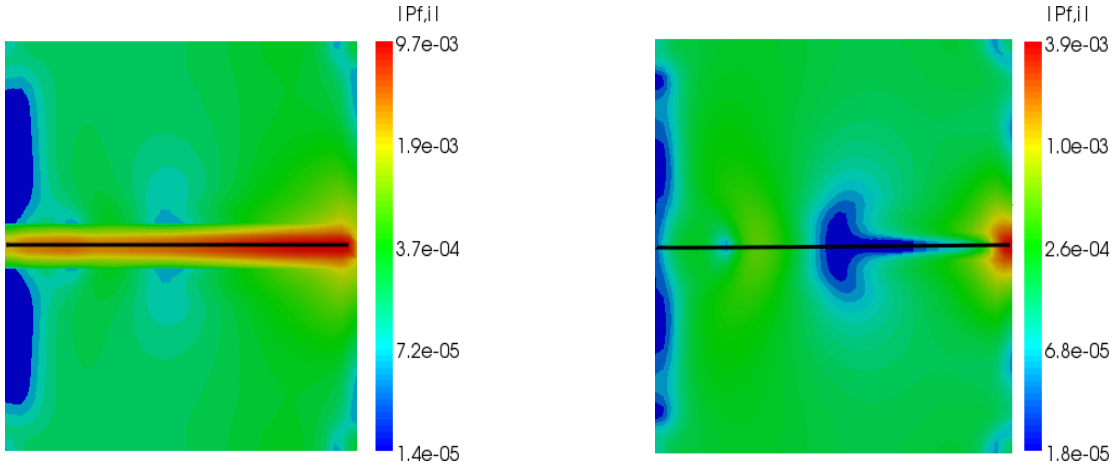

(a) (b)

Figure 10: Norm of the pressure gradient profiles [MPa/mm]: (a) with micro-flow coupling and (b) without micro-flow coupling

Two mesh sizes, 10×100 and 5×50, have been used, each composed of quadrilateral elements. A constant time increment $\Delta t = 0.01$ s has been used.

The load-displacement diagrams are shown in Figure 6. The roughness of the load-displacement diagram of the coarser mesh is due to the fact that a discontinuity is extended through an entire element, see also [12]. When the mesh is refined the response becomes smoother. Nevertheless, the load-displacement curve that stems from the coarser mesh generally follows that of the finer mesh, indicating that the model is independent of the spatial discretisation.

7.2. Delamination test

This problem has been analysed previously in Reference [9] for an unsaturated porous medium and using a small-strain assumption. The problem is reanalysed here, assuming a fully saturated medium, but extending to a finite strain framework. The notched square plate has a length 50 mm and is located along the symmetry axis. The geometry and loading of the plate are shown in Figure 7. The plate is loaded in pure mode-I by two vertical velocities $\dot{u} = 2.35 \times 10^{-3}$ mm/s. All boundaries of the plate are assumed to be impermeable. The analysis is carried for a discretisation of 45×45 bilinear quadrilateral elements with time steps of 0.01s. The numerical analysis continues until the crack tip has

reached the right-hand side of the plate.

Figure 8 shows the load-displacement diagram. Figure 9 shows the contours of the pressure. Two cases are shown, first for a simulation that includes the micro-flow coupling term at the interface, and secondly, a simulation is shown in which the micro-flow coupling term is not taken into account. In the latter case, the crack is clearly not recognized as a discontinuity in the pressure field and the fluid flows through the crack as it does in the bulk. Another representation of the effect is given in Figure 10, which displays the norm of the pressure gradient.

7.3. Shear test

The model can capture crack propagation in arbitrary directions, which is demonstrated by the shear test on a fluid-saturated beam-like structure shown in Figure 11. A 10 mm pre-notch is located at the symmetry axis of the beam. The beam is clamped on the right hand side, while the top and bottom sides are simply supported. The boundaries of the beam are assumed to be impervious. The lower-left side of the beam is loaded in pure mode II-by horizontal velocities $\dot{u} = 1.0 \times 10^{-3}$ mm/s, while the upper-left side is clamped. Two meshes, with 2480 and 7650 elements, respectively, have been used, each composed of quadrilateral elements. A constant time increment $\Delta t = 0.01$ s has been used. The mode-II loading is sustained until the crack reaches the beam edge.

Figure 7.3 shows the fluid pressure profile as the crack propagates while Figure 7.3 shows the norm of the pressure gradient during crack propagation. The highest gradient of the pressure occurs where the crack opens. The crack path is plotted in Figure 7.3. Evidently, the crack deviates earlier for the finer discretisation. However, during propagation a similar path is followed for both mesh sizes, which indicates mesh independency.

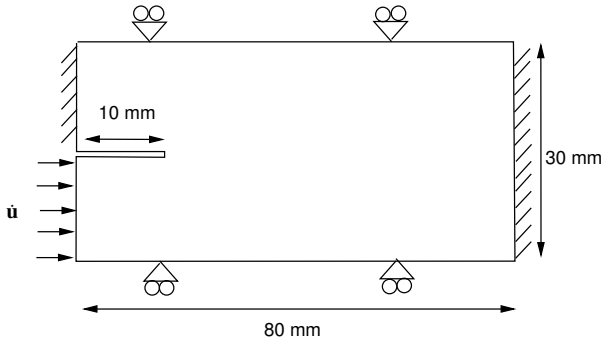

Figure 11: Shear test geometry for two square plate porous material with a 10 mm crack notch.

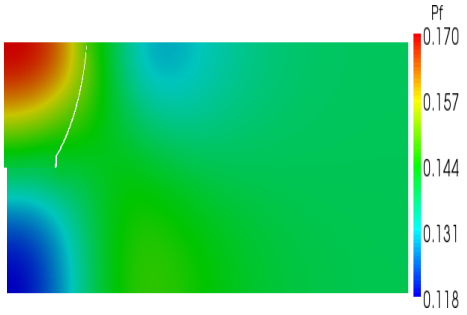

Figure 12: Fluid pressure profiles [MPa] for shear test

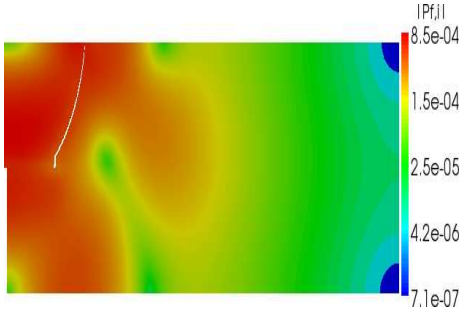

Figure 13: Norm of fluid pressure profile [MPa/mm] for shear test

8. Conclusions

A large-strain formulation has been developed for a fluid-saturated porous medium, which contains cracks, either pre-existing or nucleating and propagating. The location and the direction of the cracks is independent of the discretisation by virtue of the exploitation of the partition-of-unity property of finite element shape functions. The fluid in the cracks has been assumed to be viscous, and the permeability in the cracks has been assumed to be depending on the crack opening, but these restrictions can be relaxed without major consequences. Also, the elaboration, which has been done for two dimensions, can straightforwardly be generalised to three dimensions. The subgrid scale model generates the coupling conditions for mass and momentum to the governing equations at the macro-scale. The example calculations demonstrate the importance of the inclusion of the coupling conditions.

9. References

[1] K. Terzaghi, *Theoretical Soil Mechanics*, Wiley, New York, 1943.

[2] M.A. Biot, *General theory of three-dimensional consolidation*, J. Appl. Phys. **12** (1941) 155-164.

[3] A. Verruijt, *Computational Geomechanics. Theory and Application of Transport in Porous Media*, Kluwer Academic Publishers, Dordrecht, 1995.

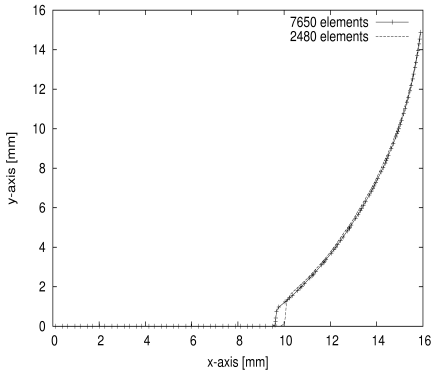

Figure 14: Comparison of the crack path for two different number of elements

[4] W.J. Vankan, J.M. Huyghe, D.W. Slaaf, C.C. van Donkelaar, M. Drost, J.D. Janssen, A. Huson, *Finite element simulation of blood perfusion in muscle tissue during compression and sustained contraction*, Am. J. Physiol. 273 (1997) H1587-H1594.

[5] C.W.J. Oomens, D.H. van Campen, H.J. Grootenboer, *A mixture approach to the mechanics of skin*, J. Biomech. **20** (1987) 877-885.

[6] K. Malakpoor, E.F. Kaasschieter, J.M. Huyghe, *Mathematical modelling and numerical solution of swelling of cartilaginous tissues, part I: Modeling of incompressible charged porous media*, ESAIM: Mathematical Modelling and Numerical Analysis 41 (2007) 661-678.

[7] R. de Borst, J. Rethoré, M.A. Abellan, *A numerical approach for arbitrary cracks in a fluid-saturated porous medium*, Arch. Appl. Mech. **75** (2006) 595-606.

[8] J. Rethoré, R. de Borst, M.A. Abellan, *A discrete model for the dynamic propagation of shear bands in fluid-saturated medium*. Int. J. Numer. Anal. Meth. Geomech. **31** (2007) 347-370.

[9] J. Rethoré, R. de Borst, M.A. Abellan, *A two-scale model for fluid flow in an unsaturated porous medium with cohesive cracks*, Comp. Mech. **42** (2008) 227-238.

[10] I. Babuska, J.M. Melenk, *The partition of unity method*, Int. J. Numer. Meth. Engng. **40** (1997) 727-758.

[11] N. Moës, J. Dolbow, T. Belytschko, *A finite element method for crack growth without remeshing*, Int. J. Numer. Meth. Engng. **46** (1999) 131-150.

[12] G.N. Wells, L.J. Sluys, *A new method for modelling cohesive cracks using finite elements*, Int. J. Numer. Meth. Engng. **50** (2001) 2667-2682.

[13] G.N. Wells, R. de Borst, L.J. Sluys, *A consistent geometrically nonlinear approach for delamination*, Int. J. Numer. Meth. Engng., **54** (2002) 1333-1355.

[14] J.J.C. Remmers, R. de Borst, A. Needleman, *A cohesive segments method for the simulation of crack growth*, Comp. Mech. **31** (2003) 69-77.

[15] J.M. Huyghe, M.M. Molenaar, F.P.T. Baaijens, *Poromechanics of compressible charged porous media using the theory of mixtures*, J. Biomech. Eng. 129 (2007) 776-785.

[16] E. Detournay, A.H.D. Cheng, *Fundamentals of poroelasticity*, Vol. II, Anal. Design Method, C. Fairhurst (Ed.), Pergamon Press (1993) pp. 113-171.

[17] X.P. Xu, A. Needleman, *Numerical simulations of fast crack growth in brittle solids*, J. Mech. Phys. Solids **42** (1994) 1397-1434.

[18] T. Belytschko, W.K. Liu, B. Moran, *Nonlinear finite elements for continua and structures*. Wiley, Chichester, 2000.

[19] R.W. Lewis, B.A. Schrefler, *The Finite Element Method in the Static and Dynamic Deformation and Consolidation of Porous Media* (2nd Ed). Wiley, Chichester, 1998.

[20] J.R. Booker, J.C. Small, *An investigation of the stability of numerical solutions of Biot's equations of consolidation*. Int. J. Sol. Struct. **11** (1975) 907-917.

[21] G.T. Camacho, Ortiz M *Computational modeling of impact damage in brittle materials*, Int J Solids Struct **33** (1996) 12671282.